ACS APPLIED MATERIALS & INTERFACES

Research Article

www.acsami.org

Metal–Support Interaction in Platinum and Palladium Nanoparticles Loaded on Nitrogen-Doped Mesoporous Carbon for Oxygen Reduction Reaction

Lorenzo Perini,[†] Christian Durante,*[,†] Marco Favaro,[†] Valentina Perazzolo,[†] Stefano Agnoli,[†] Oliver Schneider,[‡] Gaetano Granozzi,[†] and Armando Gennaro[†]

[†]Department of Chemical Sciences, University of Padua, Via Marzolo 1, 35131 Padova, Italy

[‡]Physik Department E 19, Institute of Informatics VI, Technische Universität München, Schleißheimerstr. 90a, 85748 Garching, Germany

ABSTRACT: Mesoporous carbons are highly porous materials, which show large surface area, chemical inertness and electrochemical performances superior to traditional carbon material. In this study, we report the preparation of nitrogen-doped and undoped mesoporous carbons by an optimized hard template procedure employing silica as template, sucrose and ammonia as carbon and nitrogen source, respectively. Surface area measurements assert a value of 900 and 600 $m^2\ g^{-1}$ for the best doped and undoped samples, respectively. Such supports were then thoroughly characterized by surface science and electron microscopy tools. Afterward, they were decorated with Pt and Pd nanoparticles, and it was found that the presence of nitrogen defects plays a significant role in improving the metal particles dimension and dispersion. In fact, when doped supports are used, the resulting metal nanoparticles are smaller (2–4 nm) and less prone to aggregation. Photoemission measurements give evidence of a binding energy shift, which is consistent with the presence of an electronic interaction between nitrogen atoms and the metal nanoparticles, especially in the case of Pd. The catalytic properties of electrodes decorated with such catalyst/support systems were investigated by linear sweep voltammetry and by rotating disk electrode measurements, revealing excellent stability and good activity toward oxygen reduction reaction (ORR). In particular, although Pd nanoparticles always result in lower activity than Pt ones, both Pt and Pd electrodes based on the N-doped supports show an increased activity toward ORR with respect to the undoped ones. At the same mass loading, the Tafel slope and the stability test of the Pt@N-doped electrocatalysts indicate superior performances to that of a commercial Pt@C catalysts (30 wt % Pt on Vulcan XC-72, Johnson Matthey).

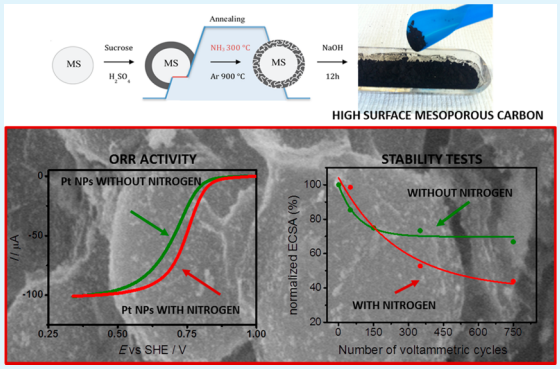

KEYWORDS: *mesoporous carbon, electrocatalysis, palladium, platinum, nitrogen doping, oxygen reduction reaction*

1. INTRODUCTION

Fuel cells and metal–air batteries are promising technologies, especially for automotive industries, due to their high energy densities, low operating temperature and environmental compatibility.[1,2] It is well-known that the slow kinetics of the oxygen reduction reaction (ORR) at the cathode limits the efficiency of fuel cells and metal–air batteries. So far, only platinum-based electrocatalysts have been found to be effective in final devices. However, Pt is expensive and its abundance in nature is not sufficient to sustain a widespread commercialization of fuel cells and metal–air batteries. Therefore, the synthesis of platinum-free electrocatalysts or the preparation of electrocatalysts with much lower content of the precious metal, preserving at least the same catalytic activity, is a current strategic issue. A viable way to reach the latter goal deals with the synthesis of new electrode support materials able to enhance the catalytic activity of the metal phase, while preserving the chemical and mechanical stability. In fact, the nature of the supports has a strong influence on some important properties of the catalyst, such as dispersion of the active phase, inhibition of sintering and loss of the catalyst during operation,[3,4] morphology of the metallic crystallites[5] and electrochemically active area.[6,7]

In recent years, there has been a growing interest in the synthesis of mesoporous carbon (MC) materials with well-controlled and well-defined morphologies and nanostructures.[8] MCs are promising materials because of their large surface area, tunable pore structure, uniform and adjustable pore size, mechanical stability, good conductivity and electrochemical performances superior to traditional carbon materials such as Acetylene Black, Vulcan XC-72R or Ketjen Black. Most of the known MCs have highly hydrophobic surfaces and a limited

Received: October 8, 2014
Accepted: December 19, 2014
Published: December 19, 2014

DOI: 10.1021/am506916y
ACS Appl. Mater. Interfaces 2015, 7, 1170–1179

number of specific active sites, which hinder their practical application as catalytic supports. It is well established in literature that the presence of a certain amount of surface oxygen groups can decrease the hydrophobicity of the carbon material, thus making its surface more accessible to the metal precursor during impregnation with aqueous solutions.[9,10] By doping with heteroatoms, the physical and chemical properties of carbon can be modified and new sites can even be created, which make the tailoring of the catalytic properties possible.[11] Among the various surface modification methods, nitrogen doping is currently in the spotlight because it is supposed that nitrogen induces a beneficial change on both the electronic and structural properties of the carbon supports. For example, changes in the surface polarity, electronic conductivity and electron-transfer tendency have been demonstrated to be beneficial to build improved electrode materials.[12] Furthermore, N-doped carbons resulted in some ORR catalytic activity even in the absence of metal loading, and even better performance and stability when mixed with Pt or non-Pt catalysts.[13−18]

In this work, we report the optimized synthesis of undoped and N-doped MCs (NMC) and their subsequent decoration with Pt or Pd nanoparticles (NPs). Sucrose and ammonia were used as sources of carbon and nitrogen, respectively, whereas Pd has been chosen as a possible substitute candidate for Pt as the active phase. The MC and NMC supports were thoroughly characterized by surface science and electron microscopy tools. The electrochemical activity toward ORR of the various materials, before and after Pd or Pt NPs decoration, was evaluated by linear sweep voltammetry using a rotating disk electrode setup. The effects of N-doping on the electrocatalytic activity are discussed.

2. EXPERIMENTAL SECTION

2.1. Chemicals. Mesoporous Silica (MS) (200 nm particle size, 4 nm pore size), sucrose (>99.5%), $PtCl_2$ (>99.9%), $PdSO_4$ (>98%), Nafion (5 wt % in EtOH) and $NaBH_4$ were purchased from Sigma-Aldrich and used as received without further purification.

2.2. Syntheses. MC samples were synthesized through impregnation of a P200 mesoporous silica template (1 g) with sucrose (1 g) and sulfuric acid (0.12 g), in water solution (5 mL). The mixture was dried in an oven at 100 °C for 6 h and then the temperature was increased to 160 °C overnight. During this pretreatment step, the carbonization starts and the color of the sample turned from white to brown. The powder was subsequently heated in a quartz tube to 900 °C for 5 h in Ar atmosphere to reach the complete carbonization of the sample. To optimize the synthesis, several heating rates from 2 to 20 °C min^{-1} were tested.

The synthesis procedure for the NMCs is quite similar to the synthesis described above for the MCs. In this case, after the pretreatment, the temperature was not increased directly to 900 °C but a new step at 300 °C for 4 h under flow of pure ammonia was introduced. After the final heat treatment for both MC and NMC, the silica content was removed by dissolution with NaOH (1 M) solution in EtOH/H_2O (50% v/v) for 24 h under vigorous stirring.

Pt or Pd NPs were loaded by reduction of the corresponding metal salts with $NaBH_4$ on MCs and NMCs. Initially, 5 mg of MC was dispersed in 2 mL of bidistilled water, then the metal salts solution (10 mg in 1 mL EtOH/H_2O mixture 1/1 v/v) was added dropwise to the suspension under stirring). After 2 h at room temperature (r.t.), 1 mL of $NaBH_4$ was added and the solution was kept under stirring for 12 h to complete the reaction. The mixture was filtered on a nylon filter membrane (pore size 0.22 μm, Sigma-Aldrich), washed with bidistilled water and dried at 80 °C for 4 h.

2.3. Electrochemical Tests. The electrochemical activity measurements were carried out by cyclic voltammetry (CV) and rotating disk electrode (RDE) voltammetry, using an EG&G PAR Model 273/A potentiostat. A conventional three-electrode configuration consisting of a glassy carbon (GC) electrode with an area of 0.071 cm^2 as the working electrode, Pt as the counter electrode, and a satured calomel electrode (SCE) as the reference electrode, was used. The GC was polished to a mirror finish with silicon carbide papers of decreasing grain size (Struers, grit: 500, 1000, 2400, 4000) followed by diamond paste (3, 1, 0.25 μm particle size).

The catalyst inks were prepared by adding 2.5 mg of M@MC or M@NMC (M = Pd, Pt) in 2.5 mL of Nafion (5% in EtOH, Sigma-Aldrich) solution via ultrasonication for 10 min. Then 10 μL of suspension was carefully pipetted onto the clean GC electrode. After that, it was dried in air at room temperature for at least 8 h. For comparison, inks based on a commercial Pt catalyst (30 wt % Pt on Vulcan XC-72, Johnson Matthey) were used as a benchmark for both (N)MC-derived Pt and Pd catalysts.

The LSV and RDE study was carried out in 0.1 M H_2SO_4, and the solutions were purged with Ar before each measurement, whereas for the ORR test, the electrolyte was bubbled with high-purity O_2 gas for at least 30 min to ensure O_2 saturation. The determination of the number of transferred electrons was measured via the ring rotating (Pt) disk (GC) electrode (RRDE) technique (Metrohm Italiana Srl). The RRDE (disk diameter 5 mm), with a collection efficiency of 25%, was prepared by dropcasting 50 μL of the catalyst ink onto the surface of the GC disk with a Hamilton microliter syringe. The electrode was dried at ambient temperature for 12 h prior to immersion into the electrochemical cell for data acquisition.

2.4. Characterization. The specific surface areas of the samples were calculated by a multipoint Brunauer−Emmett−Teller (BET) analysis of the nitrogen adsorption/desorption isotherms, whereas the pore size distribution curves were derived from the Barret−Joyner−Halenda (BJH) method (for mesopores) and the Horvath−Kawazoe (HK) method (for micropores), by using the adsorption/desorption branches.

X-ray photoemission spectroscopy (XPS) measurements were performed in an UHV chamber (base pressure < 5×10^{-9} mbar), equipped with a double anode X-ray source (PSP), a hemispherical electronanalyzer (VG Scienta) at r.t., using nonmonochromatized Mg Kα radiation ($h\nu$ = 1253.6 eV) and a pass energy of 50 and 20 eV for the survey and the single spectral windows, respectively. The calibration of the Binding Energy (BE) scale was carried out using Au 4f as reference (BE Au 4f = 84.0 eV).

For the characterization of the NMCs, the nitrogen amount was determined by normalizing the intensity of the N 1s XPS peak to the integrated area of the C 1s photoemission peak (both corrected for the differential cross section and inelastic mean free path of photoelectrons), obtaining a nitrogen concentration of 5.7 at% for the best sample (see below). The XPS peaks of carbon and nitrogen were separated into single chemical shifted components (after Shirley background removal), using symmetrical Voigt functions; the χ^2 was minimized by the use of a nonlinear least-squares routine.

To perform XPS measurements, 2.5 mg of the M@MC or M@NMC powders was dispersed in 50 μL of toluene and then gently sonicated (for 5 min) in order to efficiently disperse the powders; the solutions were then drop-casted onto electropolished polycrystalline copper or GC substrates (with a surface area of 1 cm^2). Thereafter, the samples were first dried overnight under nitrogen flux to obtain homogeneous films; then they were vacuum-dried for 2 h at about 10^{-6} mbar.

For the Raman characterization, we used a ThermoFisher DXR Raman spectrometer. All spectra were recorded using a laser with an excitation wavelength of 532 nm (1.5 mW), focused on the sample with a 50× objective (Olympus). Thermogravimetric analysis (TGA) was carried out with a Q5000IR TGA instrument (TA Waters). The samples were exposed to air and their mass was recorded while the temperature was raised from r.t. to 1000 °C. After the complete oxidation of the carbon structure to gaseous products, metal and silica residues were left.

Scanning electron microscopy (SEM) and transmission electron microscopy (TEM) images were obtained using a Zeiss Supra 35VP

DOI: 10.1021/am506916y
ACS Appl. Mater. Interfaces 2015, 7, 1170−1179

Gemini scanning electron microscope operating at 5 kV and a FEI Tecnai G2 transmission electron microscope operating at 100 kV.

3. RESULTS AND DISCUSSION

3.1. Characterization of MCs and NMCs. The samples investigated in the present paper are reported in Table 1, where also the different experimental conditions to obtain them are specified together with the data obtained by BET and BJH. The nitrogen-adsorption isotherms of MC prepared with a temperature ramp of 2 °C min^{-1} (MC-2) are presented in Figure 1a:

Table 1. BET Surface Area and Pore Structure Parameters of Different MCs and NMCs

sample[a]	BET surface area (m^2/g)	pore volume (cm^3/g)	BJH pore size (nm)	H–K pore size (nm)
MC-2	914	0.30	3.1	1.2
MC-5	857	0.31	3.1	0.9
MC-10	856	0.31	3.2	1.1
MC-20	765	0.27	3.1	1.0
NMC-2	608	0.29	3.0	0.9

[a]Numbers stand for the heating rate express in °C min^{-1}.

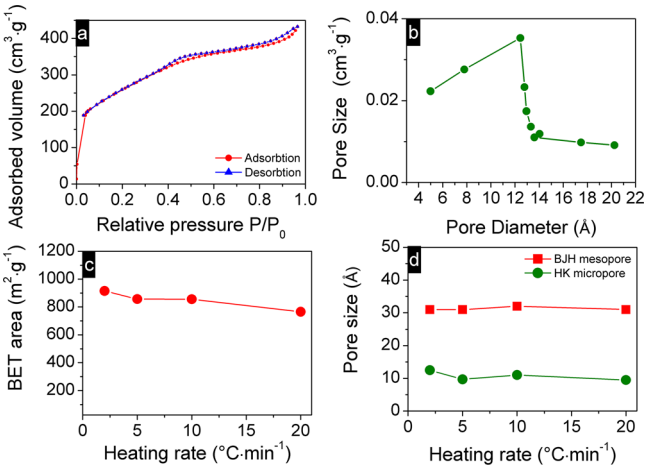

Figure 1. (a) Nitrogen adsorption/desorption isotherms of MC pyrolized at 2 °C min^{-1}; (b) BJH pore-size distribution in MC-2; (c) BET areas at different heating rates; (d) BJH and HK pore size distribution at different heating rates. The fitting error associated with the employed DFT model is less than 0.3%.

according to IUPAC classification, the isotherms are of type IV. The hysteresis is indicative of the presence of mesopores (2–50 nm diameter), whereas the pore size distribution can be calculated from the BJH adsorption isotherm reported in Figure 1b. The specific BET surface area, specific pore volume (V_p) and the pore diameters (D_p) of the MC-2 are summarized in Table. 1, along with the other MCs obtained in different experimental conditions. MC-2 exhibits 914 m^2 g^{-1} of ultrahigh specific BET surface area and 3.0 cm^3 g^{-1} of specific pore volume. The BJH method (Figure 1b) furnishes an average pore diameter of mesopores and micropores around 3 and 1 nm, respectively (Table 1). Figure 1c,d show the effect of the temperature scan rate on the surface area and pore size distribution. Although the specific surface area (Table 1) decreases from 914 to 765 m^2 g^{-1} (16.3%) with the increase of heating rate from 2 to 20 °C min^{-1}, the average pore diameter of mesopores and micropores is constant with a value around 3 and 1 nm, respectively (Figure 1d). This means that the number of pores is the parameter varying with the heating rate: at low heating rate the number of pores results to be higher than the one obtained under higher heating rates.

On the basis of these observations, N-doped mesoporous carbon (NMC-2) was prepared at a low heating rate in the very same experimental conditions as MC-2, but an additional step was inserted where ammonia was allowed to flow at 300 °C. NMC-2 exhibits an isotherm type IV (IUPAC), corresponding to a BET surface area of 608 m^2 g^{-1} and meso- and micropores of similar size as in MC-2 (Table 1). The NMC-2 surface area is only 2/3 of the one of MC-2; however, it is still much higher than that of the commercial standard Vulcan XC-72R (222 m^2 g^{-1}).[19] Because the pore structure parameters of NMC-2 and MC-2 are similar (Table 1), a possible explanation of this BET surface area reduction upon N-doping, could be referred to a partial collapse of the silica pores structure after ammonia reaction with silica. In fact, the collapse of the structure upon the template removal would end up in a general loss of the number of pores.

The SEM images of MC-2 and NMC-2 are presented in Figures 2a,b, respectively. Both samples consist of hollow

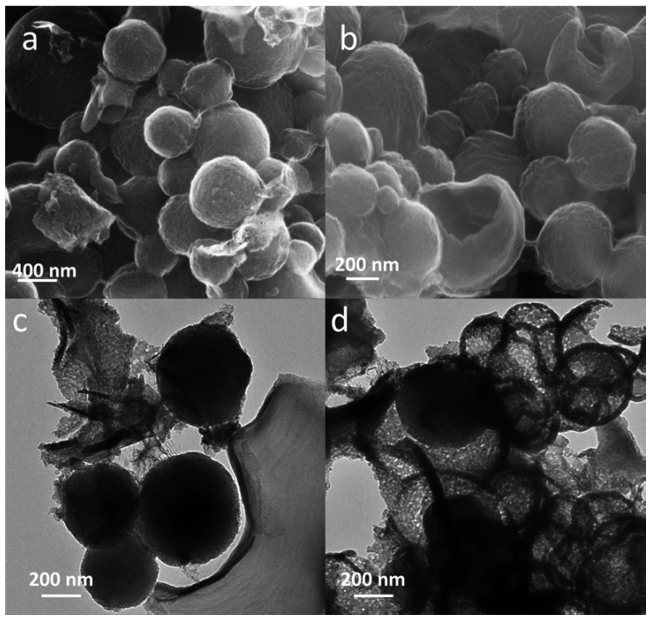

Figure 2. Representative SEM images for (a) MC-2 and (b) NMC-2. (c, d) TEM images of NMC-2.

spherical carbon particles, as good replica of the templating silica, along with other collapsed and fractured particles that give rise to a heterogeneous morphology. The average diameter of the spheres is about 300–400 nm. A more detailed structural study of NMC-2 was carried out with TEM measurements, which point out the presence of spherical carbon particles (Figures 2c,d). Pores are randomly located to construct the whole sphere, achieving a loosely packed nanostructure. In fact, several three-dimensionally interconnected bright spots can be observed on the sphere surfaces indicating the presence of mesopores, whereas the dark contrast that characterizes the edges confirms their hollow nature (Figure 2d).

To characterize the surface chemistry of the studied systems, we carried out an XPS investigation. Figures 3a,b report wide range measurements acquired for MC-2 and NMC-2 samples,

DOI: 10.1021/am506916y
ACS Appl. Mater. Interfaces 2015, 7, 1170–1179

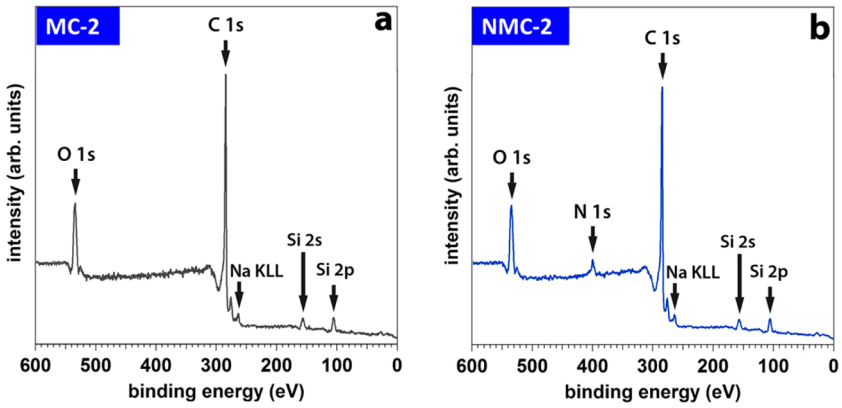

Figure 3. XPS survey spectra for (a) MC-2 and (b) NMC-2.

Table 2. Elemental Analysis Derived from XPS Measurements, for MC-2 and NMC-2

	Si ($\%_{at}$)	Na ($\%_{at}$)	C ($\%_{at}$)	N ($\%_{at}$)	O ($\%_{at}$)
MC-2	4.1	0.8	80.3		14.8
NMC-2	3.7	0.8	75.8	5.7	14.0

respectively, and the corresponding elemental surface stoichiometries are reported in Table 3. Both survey spectra exhibit the photoionization peaks of C 1s (284.6 eV) and O 1s (533.7 eV) core levels, whereas only NMC-2 samples show the N 1s photoemission peak (399.4 eV). The nitrogen concentration in NMC-2 is 5.7 at. % (Table 2). Furthermore, XPS reveals traces of contamination from the templating silica and from the concentrated NaOH solution used to dissolve the templating agent. The trace of silica can be completely removed by a prolonged washing in EtOH/NaOH solution followed by the rinse with abundant bidistilled water.

To get a more precise description of the chemical identity of the functional groups present on MC-2 and on NMC-2, the C 1s and N 1s energy regions were acquired at high resolution and the corresponding peaks were fitted with Voigt functions, imposing a full width at half-maximum (FWHM) in the range of 1.0−1.4 eV. Figure 4 reports the multipeak analysis of the C 1s and N 1s signals for MC-2 and NMC-2, together with ball and stick models of the different chemical species identified. Concerning MC-2, we can distinguish five different components in the deconvolution of the C 1s photoemission spectrum: the main component (which constitutes 72% of the signal), centered at 284.5 eV, represents the sp^2-hybridized carbon (Csp^2) forming the graphitic lattice. The component centered at 285.5 eV is due to sp^3-hybridized carbon (Csp^3), which constitutes tetragonally coordinated carbon clusters and C—H bonds,[20,21] while the third and fourth components at 286.4 and 288.0 eV, respectively, are related to C—OH bonds and carbonyl (−C═O) groups. For a correct fitting procedure, it is also necessary to introduce a small component in the low-energy tail, which is related to C atoms around vacancy sites (BE = 283.7 eV).[22]

Interestingly, the C 1s spectrum of NMC-2 (Figure 4c) shows a significant increase of the Csp^3 component, which can be associated with the formation of amorphous carbon. In fact, this side reaction is promoted by the low temperature treatment in ammonia (4 h, 300 °C), performed on the MC precursor in order to obtain the N-doping. Concerning the component centered at 286.4 eV, it is not possible to distinguish the contribution of the C—OH groups from that of the C—N bonds, which are known to give a characteristic signal centered at 286.6 eV.[23] Moreover, the carbonyl component at 288.0 eV overlaps that of the −N—C—OH groups.[24] The new component at the high BE tail (BE = 289.0 eV) can be related to the presence of strong electron-withdrawing groups, such as formamide-like fragments (−N—C═O).[24] Table 3 summarizes the results and makes a comparison between the fits of the different C 1s spectra.

The nitrogen functional groups characterization was carried out by analyzing the N 1s XPS signals, as reported in Figure 4d. Seven different components were identified,[25] with the main peaks centered at 398.1, 399.0, 400.3 and 401.2 eV, which can be described as pyridinic groups,[24,26] amine groups,[22,24] pyrrolic groups[25] and graphitic N,[25] respectively. According to the literature, in order to fit a curve consistently with the experimental data, we added three components centered at 402.5, 403.7 and 404.8 eV, in the high-energy tail of the N 1s spectrum. These are associated with quaternary nitrogen groups (402.5 eV), N—C—OH[27] and N—C═OH[27] groups (403.7 eV), and highly oxidized nitrogen groups[27] (404.8 eV), such as NO_x groups, even though in limited amount.

Figure 5 compares Raman spectra of MC-2 and NMC-2; the analysis of the peak positions and intensities gives information

Table 3. Results of the Fitting Procedure Performed on the C 1s Spectra Related to MC-2 (left) and NMC-2 (right)[a]

MC-2	A_i/A_{tot} (%)	NMC-2	A_i/A_{tot} (%)
C vacancy (BE = 283.7 eV, Δ = 1.3 eV)	6.6	C vacancy (BE = 283.7 eV, Δ = 1.3 eV)	6.8
Csp^2 (284.5 eV, Δ = 1.3 eV)	72.3	Csp^2 (BE = 284.5 eV, Δ = 1.3 eV)	57.3
C—H (Csp^3) (BE = 285.5 eV, Δ = 1.1 eV)	11.8	C—H (Csp^3) (BE = 285.5 eV, Δ = 1.2 eV)	16.4
C—OH (BE = 286.4 eV, Δ = 1.3 eV)	7.1	C—OH/C—N bonds (BE = 286.5 eV, Δ = 1.3 eV)	14.7
C═O (BE = 288.0 eV, Δ = 1.2 eV)	2.2	C═O/−N—C—OH (BE = 288.0 eV, Δ = 1.3 eV)	2.7
		−N—C═O (BE = 289.0 eV, Δ = 1.2 eV)	2.1

[a]The percentages of each single component are normalized to the total integrated area of the C 1s spectrum. Δ is the FWHM of each component.

DOI: 10.1021/am506916y
ACS Appl. Mater. Interfaces 2015, 7, 1170−1179

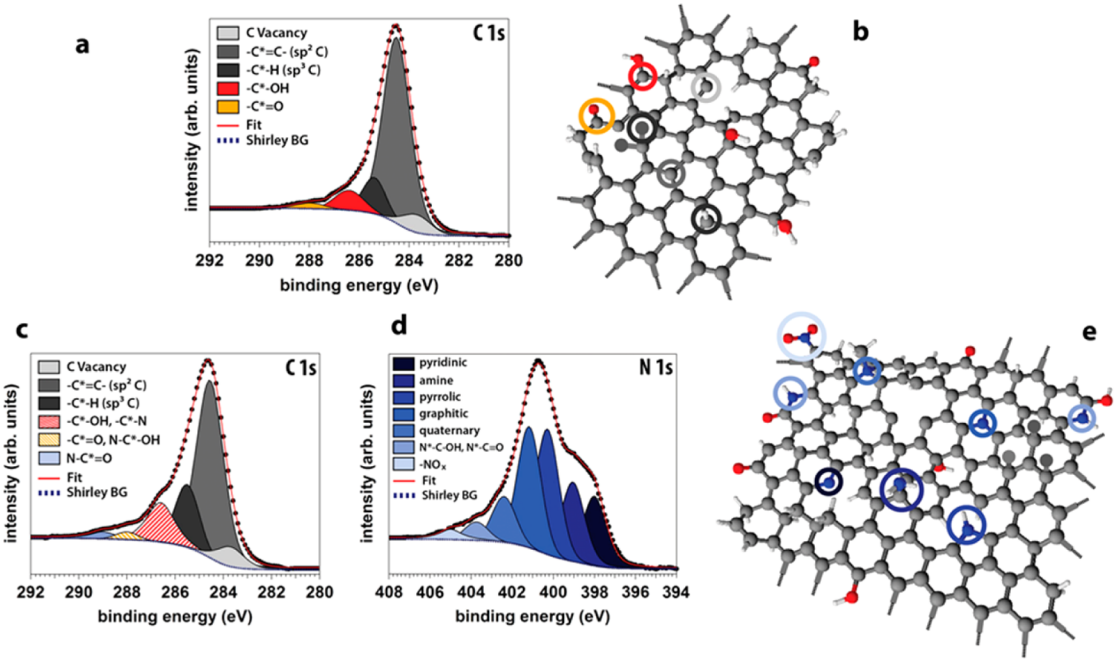

Figure 4. XPS detailed study of (a) MC-2 and (c, d) NMC-2. Modeling of the surface functional groups (b) MC and (e) NMC.

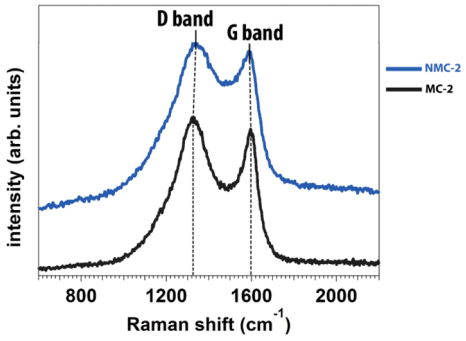

Figure 5. Raman spectra for MC-2 and NMC-2.

about the changes of the atomic structure of the samples. The two intense bands observed at 1600 and at 1325 cm^{-1} are the G band[28] (tangential vibration mode, E_{2g} symmetry group) and the D band,[28] also known as disorder vibration mode (belonging to the A_{1g} symmetry group), respectively. The latter is observable only in the presence of defects that lead to a local breakdown of the D_{6h} symmetry of the graphitic honeycomb lattice[28] (such as sp^3 carbon or dopant atoms). Compared to undoped MC, the NMC sample shows a significant increase in structural disorder, as evidenced by the increase and the broadening of the D band. This is in agreement with the previous XPS observations; in fact, the evolution of the D band with the doping is due to both the increase of the Csp^3 and the doping of the carbon structure. Moreover, it is found that in NMC-2 the G band shifts from 1593 to 1589 cm^{-1} and the D band moves from 1330 to 1321 cm^{-1} in comparison to those of the mesoporous carbon MC-2, which can be ascribed to the incorporation of nitrogen into the carbon matrix.[29]

3.2. Characterization of Metal Loaded-MC and NMC.

Nanoparticles from different metal salts ($PdSO_4$, $PtCl_2$) were loaded on undoped (Pd@MC-2, Pt@MC-2) and doped (Pd@NMC-2, Pt@NMC-2) samples by a simple chemical reduction method with sodium borohydride ($NaBH_4$) as the reducing agent. TEM images of Pt@MC-2 (Figure 6a) and Pt@NMC-2 (Figure 6c) clearly show that Pt NPs with high loading are uniformly dispersed throughout the samples. The corresponding particle size distribution histograms (Figures 6b,d) were obtained by calculating the size of more than 50 randomly selected particles in the magnified TEM images. For Pt@MC-2 and Pt@NMC-2 samples, the mean Pt particle size diameter is ca. 1.7 and 1.3 nm, respectively, and the NPs were well dispersed on the surface of pristine and doped MC. However, the formation of some Pt aggregates (>8 nm) can be clearly seen, especially in the case of Pt@MC-2, suggesting that the nitrogen surface doping is helpful to stabilize Pt NPs on Pt@NMC-2. Regarding Pd NPs supported on MC-2 (Figure 6e), the size distribution histogram (Figure 6f) shows an average diameter of ca. 5−6 nm. When Pd NPs nucleate and grow on NMC-2 (Figure 6g), the particle size diameter decreases to 2−3 nm (Figure 6h). In this case, Pd agglomerates are still present though to a lesser extent than in Pd@MC-2. It is evident that the presence of homogeneously distributed nitrogen functional groups can provide nucleation sites and thus promote a higher dispersion of metal NPs. Furthermore, nitrogen doping results in an improvement of hydrophilicity and wettability of NMC-2. The enhanced access of solvated and charged metal precursor ions to the NMC-2 surface can be associated with the superior dispersion of metal NPs and it effectively prevents agglomeration.[30] It is also known that nitrogen functional groups can increase the interaction between metal NPs and the substrate, immobilizing Pt or Pd NPs.[18,31] This has been confirmed also for Pt and Pd NPs deposited on N-doped HOPG[4,32,33] CNTs[30] and N-doped GC.[5] Figure 7 reports the XPS Pd 3d and Pt 4f spectral regions of samples deposited on MC-2 and NMC-2. As can be observed, the photoemission spectra of the metals show significant peak broadening when they are deposited on NMC-2. This can be explained by the formation of oxidized metal species over the nitrogen sites. Moreover, a BE shift of the signals takes place after the deposition on NMC-2 and this is particularly evident in the case of Pd@NMC-2 (Figure 7a). For

DOI: 10.1021/am506916y
ACS Appl. Mater. Interfaces 2015, 7, 1170−1179

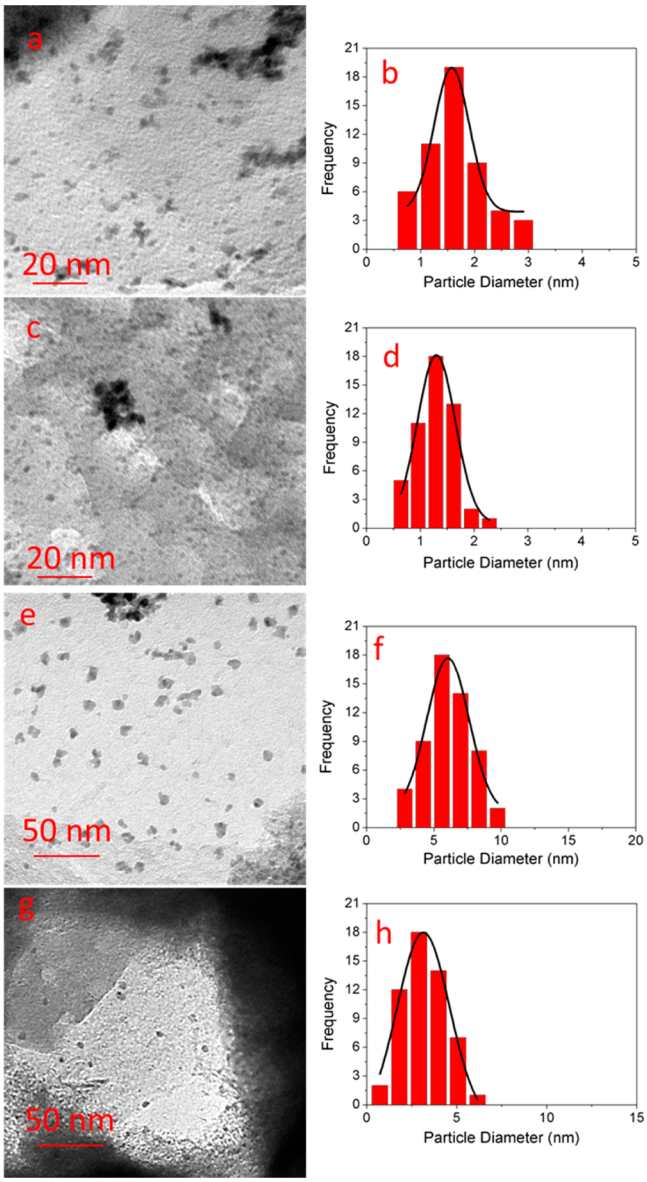

Figure 6. TEM images and size distribution of Pt@MC-2 (a and b), Pt@NMC-2 (c and d), Pd@MC-2 (e and f) and Pd@NMC-2 (g and h).

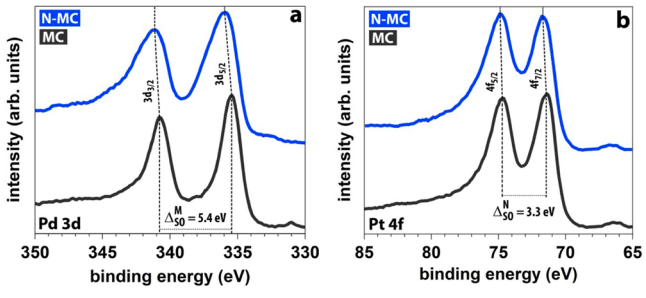

Figure 7. Pd 3d (a) and Pt 4f (b) XPS regions of M@MC and M@NMC (M= Pd, Pt).

Pt, it was reported that the addition of nitrogen to the support induces a BE shift that is proportional to the number and proximity of nitrogen atoms to the carbon−platinum bond and that it is a result of the destabilization induced by nitrogen atoms on the delocalized double bond present in the undoped structure.[31,34] Table 4 summarizes the values of BEs and FWHMs of the photoemission peaks recorded for Pt and Pd

Table 4. BE and FWHM of XPS signals of Pd and Pt deposited on MC-2 and NMC-2

	MC-2		NMC-2	
	BE (eV)	FWHM (eV)	BE (eV)	FWHM (eV)
Pd $3d_{5/2}$	335.4	1.7	336.0	2.9
Pt $4f_{7/2}$	71.3	1.4	71.6	1.7

deposited on both MC-2 and NMC-2. The metal loading was evaluated by XPS analysis to be ca. 30 wt % for each sample; this result was confirmed also by thermogravimetric analysis (TGA).

3.3. Electrochemical Analyses. The electrochemical properties of pure MC-2 and NMC-2 were examined by cyclic voltammetry (CV) in Ar purged 0.1 M H_2SO_4 solution at a scan rate of 200 mV s^{-1} (Figures 8a,b). NMC-2 shows an

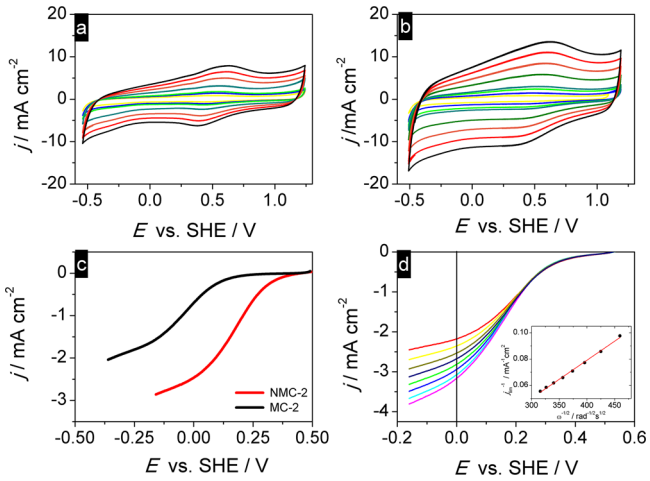

Figure 8. Cyclic voltammetry at different scan rates in 0.1 M H_2SO_4 on (a) MC-2 and (b) NMC-2. (c) RDE linear sweep voltammetry curves on MC-2 and NMC-2 modified GC electrode in O_2-saturated 0.1 M H_2SO_4 solution. Scan rate 10 mV s^{-1}. (d) RDE linear sweep voltammetry curves on NMC-2 at different rotation rates in the range 1000−3100 rpm/s in O_2-saturated 0.1 M H_2SO_4 solution at scan rate of 10 mV s^{-1}. The inset reports the corresponding Koutecky−Levich plot at 0.0 V vs SHE.

increased capacitance with respect to MC-2; it is commonly known that nitrogen doping improves the capacitive behavior of carbon materials and this is generally attributed to the electron donor capability of nitrogen atoms.[35,36] Specifically, the strong electron donor nature of nitrogen atoms promotes reinforcement in π bonding, enhancing wettability of the material at the electrode/electrolyte interface. Therefore, the presence of nitrogen functional groups induces a pseudocapacitive effect,[37] caused by the increased adsorption of proton and electrolyte ions in the electrical double layer.[38]

A well-defined quasi-reversible redox peak couple was observed on both MC-2 and NMC-2 in the potential range of 0.75 and 0.25 V vs SHE. The presence of these peaks may be ascribed to redox active surface oxygen functional groups such as hydroquinone/quinone, which usually undergo proton coupled electron transfer. This type of surface electrochemistry behavior can be found in other type of mesoporous carbon and carbon nanotubes modified electrodes.[39,40]

DOI: 10.1021/am506916y
ACS Appl. Mater. Interfaces 2015, 7, 1170−1179

The linear sweep voltammetry (LSV) with a rotating disk electrode (RDE) was undertaken at different rotating rates from 1000 to 3100 rpm in an O_2-saturated 0.1 M H_2SO_4 solution, at a scan rate of 5 mV s^{-1} in order to ensure a steady-state condition (Figure 8c). Both MC-2 and NMC-2 show mixed kinetic and mass transport control, but the influence of mass transport becomes visible at much lower potentials for MC, in a region where thermodynamically other reactions like hydrogen evolution could take place. An ideal plateau was not fully reached in these experiments but clearly approached at all rotation rates for NMC-2 (Figure 8d). NMC-2 approached the plateau of diffusion-limiting currents below −0.1 V vs SHE, and showed an onset reduction potential for O_2 at 0.33 V vs SHE almost 300 mV more positive than that of MC-2. Such a difference in the onset potential between the two materials highlights a pronounced electrocatalytic activity of NMC-2 for oxygen reduction with respect to the undoped MC-2. The improved catalytic activity of nitrogen doped carbon based electrodes toward ORR is a well-established effect although the actual mechanisms involved in the reaction are not well understood to date.[41] The effect is generally ascribed to the n-type dopant character of nitrogen, which allows a faster adsorption of oxygen molecules on carbon atoms that are next neighbors to the nitrogen doping atoms, in particular those placed in a substitutional, pyridinic or pyrrolic position.[42−46] To investigate the mechanism of the electron transfer process, we used the Koutecky−Levich (K-L) plot (Figure 8d inset), which was obtained from the polarization curves at various rotation rates (Figure 8d).

$$\frac{1}{j} = \frac{1}{j_k} + \frac{1}{j_d} = \frac{1}{nFkC_{O_2}} + \frac{1}{0.62nF(D_{O_2})^{2/3}\nu^{-1/6}C_{O_2}\omega^{1/2}} \quad (1)$$

In the K-L equation j is the measured current density, j_k and j_d are the kinetic and diffusion-limited current densities, respectively, n is the number of electrons transferred per O_2 molecule, k is the rate constant for O_2 reduction, F is the Faraday constant (96 485 C mol^{-1}), ω is the rotation rate, C_{O_2} is the concentration of oxygen in the bulk (1.1×10^{-6} mol cm^{-3}),[47] D_{O_2} is the diffusion coefficient of oxygen (1.4×10^{-5} cm^2 s^{-1})[48] and ν is the kinematic viscosity of the solution (0.01 cm^2 s^{-1}).[48] The geometric surface area (0.0706 cm^2) was considered in the calculation. The slope of the straight line (Figure 8d inset) allows us to assess the number of electrons involved in the ORR. The experimentally determined number of electrons is 3.47 at 0.0 V vs SHE for NMC-2, which indicates that the four-electron process leading directly to water is the favored reduction mechanism.

The electrochemical investigation was extended also to Pt@NMC-2 and Pd@NMC-2, and the results were compared with Pt@MC-2, Pd@MC-2 and with the commercial standard Johnson Matthey 30 wt % Pt on Vulcan XC72R (hereafter denoted as Pt@vulcan). The electrochemical properties of Pt and Pd NPs deposited on MC-2 and NMC-2 were first examined by cyclic voltammetry, as shown in Figure 9a,b. For both types of NPs, there are three distinct potential regions in the voltammograms: the hydrogen adsorption/desorption region between 0.0 and 0.25 V, the double-layer region between 0.25 and 0.50 V and the surface oxide formation/reduction region (>0.50 V). The Coulombic charge for hydrogen adsorption/desorption (Q_H) can be used to calculate the electrochemical active Pt and Pd surface area of the electrodes.[49,50] The value of Q_H (mC cm^{-2}) was calculated as

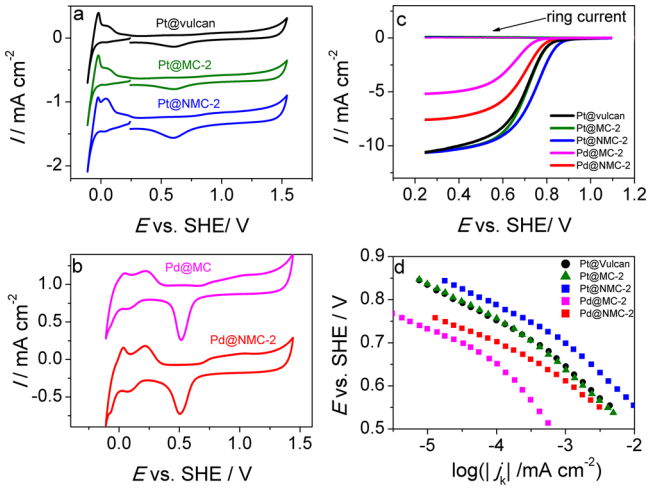

Figure 9. (a,b) Cyclic voltammetry of the electrocatalysts in an oxygen-free 0.1 M H_2SO_4, scan rate 100 mV s^{-1}. (c) RRDE linear sweep voltammetry curves on Pt@vulcan, M@MC-2 and M@NMC-2 (M = Pt, Pd) in O_2-saturated 0.1 M H_2SO_4 solution. Scan rate 10 mV s^{-1}, rotation rate 1600 rpm. (d) Mass transfer corrected Tafel plots extracted from the data of the RDE linear sweeps; the current density is normalized to the geometric surface area of the electrode.

the mean value between the amounts of charge exchanged during the electroadsorption and desorption of H_2 on Pt or Pd sites, with the correction of the capacitive current contribution. The electrochemical active surface area can therefore be calculated according to the formula:

$$\mathrm{EAS} = \frac{Q_H}{[M]\cdot q} \quad (2)$$

where [M] is the metal loading in the electrode and represents the M/C wt % determined by XPS and TGA measurements, which in the present case is 42.5 μg cm^{-2}. The factor q = 0.21 represents the charge required to oxidize a monolayer of H_2 on smooth Pt and Q_H (μC cm^{-2}) is the charge for hydrogen adsorption/desorption. Table 5 summarizes the results for the catalysts tested. The results point out that Pt@MC-2 and Pt@vulcan have similar EAS, whereas Pt@NMC-2 sample shows the higher EAS. The increase in EAS indicates that a larger fraction of the Pt surface is exposed. This in agreement with the consideration expressed in section 3.2 where it was observed that on nitrogen doped mesoporous carbon, there is a better nucleation and dispersion of Pt NPs, and less agglomeration. It is worth noting that the EAS decreases sensitively when passing

Table 5. Electrochemical Data Obtained from Cyclic and Linear Sweep Voltammetry

catalyst	E_p[ac] (V)	E_{onset}[bc] (V)	$E_{1/2}$[bc] (V)	$\Delta E_{1/2}$[bd] (mV)	n[e]	EAS[a] (m^2/g)
Pt@vulcan	0.687	0.804	0.707	0	3.93	43
Pt@MC-2	0.687	0.804	0.707	0	3.98	46
Pt@NMC-2	0.701	0.842	0.748	41	3.89	67
Pd@MC-2	0.660	0.734	0.646	−61	3.98	26
Pd@NMC-2	0.668	0.753	0.682	−25	3.86	32

[a]Data obtained from cyclic voltammetery. [b]Data obtained from RDE voltammetry. [c]All potentials are referred to SHE. [d]$\Delta E_{1/2} = E_{1/2}^{\text{catalyst}} - E_{1/2}^{\text{Pt@vulcan}}$. [e]Number of transferred electrons calculated from RRDE measurements

DOI: 10.1021/am506916y
ACS Appl. Mater. Interfaces 2015, 7, 1170−1179

from Pt to Pd NPs loaded on MC-2. This effect can be associated with the NPs dimension that in the case of Pd@MC-2 results to be 3−4 times greater than for Pt NPs, causing a decrease of the NPs surface area. However, when Pd NPs are loaded on NMC-2, it is possible to observe again an increase of the EAS, in accordance with the fact that Pd@NMC-2 shows smaller catalyst particles.

The electrocatalytic performances for the whole batch of electrocatalysts toward ORR were tested by both cyclic voltammetry and linear sweep voltammetry at RDE and RRDE. The reduction peak potentials (E_p) for the irreversible reduction of O_2 in silent condition at all the investigated surfaces are reported in Table 5. Figure 9c presents the ORR polarization curves at RRDE (1600 rpm, 10 mVs^{-1}) for Pt and Pd catalysts with different carbon supports. From the disk current response, it should be noted that the onset and the half-wave potential of Pt@MC-2 are in good agreement with the values of Pt@vulcan. Therefore, it appears that the mere increase of the carbon support surface area does not improve the mass specific catalytic activity. It is interesting to observe that Pt@NMC-2 is characterized by better performances (in terms of onset potential and E_p, Table 5) than the commercial standard Pt@vulcan; in fact the diffusion limiting current density of Pt@NMC-2 reaches that of Pt@vulcan and a positive shift of about 40 mV exists in the half-wave potential of Pt@NMC-2 as compared to Pt@vulcan (Table 5). Also in the case of Pd based catalyst, an increased catalytic activity is observed when the Pd NPs are supported on NMC-2. However, the catalytic performance is significantly worse than Pt@vulcan, especially in term of half wave potential.

The K-L plots (not shown), resulting from the polarization curves for the ORR at different rotation rates, are linear for all the investigated catalysts. This indicates a first-order dependence of the kinetics for the ORR on the Pt and Pd surface. Figure 9c reports also the ring current recorded at RRDE for all the investigated electrodes in an oxygen saturated 0.1 M H_2SO_4 solution. The ring currents were at least 2 orders of magnitude lower than the disk currents, indicating the production of minimal amounts of H_2O_2. The electron number calculated from the formula:

$$n = \frac{4I_d}{(I_d + I_r/N)}$$

where I_d is the limiting disk current, I_r is the limiting ring current, and N is the collection efficiency (0.25), shows that $n \approx 3.8-3.9$ within the range of 0.3 to 0.5 V for the commercial Pt/C as well as for the new catalysts (Table 5).

The mass transfer corrected Tafel plots for ORR activity of these samples are shown in Figure 9d. The kinetic current density of the different catalysts at various potentials can be determined according to the equation:

$$j_k = \frac{j_{lim} \cdot j}{j_{lim} - j} \quad (3)$$

In all five observed cases, double slope Tafel plots are evident, which is known to be dependent on the formation of metal oxide on the NPs surface.[51] The higher current density is observed in the case of Pt@NMC-2 catalyst, which indicates that the O_2 reduction rate is faster on Pt NPs loaded on a nitrogen-doped support. The same observation can be made in the case of Pd NPs loaded on doped MC. As it was seen above for the NMC, the presence of nitrogen defects on MC improves the catalytic performance of Pt and Pd NPs toward ORR. In terms of onset and peak potentials, the ORR activity increases as follows: Pd@MC-2 < Pd@NMC-2 < Pt@vulcan ≈ Pt@MC < Pt@NMC-2, as particularly evidenced by the $E_{1/2}$ potentials of these samples (Table 5).

3.3. Stability Tests of Pt NPs on Doped and Undoped Mesoporous Carbon. The active surface area of Pt NPs, which is determined from the hydrogen adsorption/desorption region,[49] is used in order to compare the loss rate of Pt and Pd quantitatively. In Figure 10a, the initial active area is fixed as

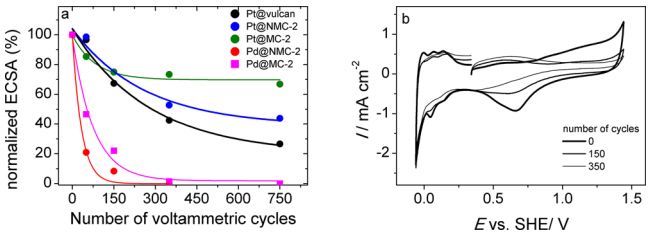

Figure 10. (a) Degeneration of the Pt and Pd active area of supported Pt particles in the stability measurements, (b) cyclic voltammograms recorded in 0.1 M H_2SO_4 solution on Pt@NMC-2 at 0, 150 and 350 voltammetric cycles, scan rate 50 mV s^{-1}.

100%, and the residual active area after potential cycles is normalized to the initial area in percentage. The residual active area versus the number of potential cycles is fitted to the exponential decay function shown as the solid lines. In Figure 10b is reported, as an example, the electrochemical behavior of Pt@NMC-2 recorded after zero, 150 and 350 potential cycles. After 750 voltammetric cycles performed between 0.25 and 1.45 V vs SHE at 50 mV s^{-1} in 0.1 M H_2SO_4 at 25 °C, a Pt@vulcan 25% of Pt active area remains, whereas the Pt@NMC-2 and Pt@MC-2 keep 44% and 67%, respectively, of initial Pt active area. In the case of Pd NPs, the active surface area decreases to the 20% of the initial value after 50 and 150 cycles for NMC-2 and MC-2, respectively. This indicates that the Pt and Pd NPs supported on doped MC have a lower stability as compared with the undoped MC, but in the case of Pt NPs, they show higher stability with respect to the commercial standard Pt@vulcan. These results may be indicative of an increased stabilization provided by the mesoporous carbon with respect to the vulcan as an electrode support. A possible rationalization of the higher stability of Pt NPs on mesoporous carbon may be done by considering the particle dimension with respect to the pore size of the supporting matrix. Pt NPs are very small (1−2 nm) and therefore, besides dissolution, Pt NPs can be subjected to Ostwald ripening.[52] This effect is less pronounced when mesoporous carbon is adopted due to a beneficial confinement effect inside the mesoporous structure. In the case of N doped MC the confinement effect could be limited on the bases of a lower number of available mesopores with respect the undoped MC, as already observed from the BET analysis.

Even though the increased stabilization expected for the interaction between Pt NPs with the nitrogen functional groups was not observed, these represent very promising and interesting results since they allow to better define the parameters influencing the catalyst activity and stability and therefore to design with a clear view carbon supports able to outclass standard commercial material both in term of activity and chemical and mechanical stability.

DOI: 10.1021/am506916y
ACS Appl. Mater. Interfaces 2015, 7, 1170−1179

4. CONCLUSIONS

N-doped mesoporous carbon with high surface area and enhanced catalytic activity toward ORR was prepared by an optimized hard template approach, employing NH_3 as the doping agent. Pd and Pt NPs were deposited by wet impregnation on both doped and undoped samples, showing that the presence of nitrogen functional groups drives the dimension and the dispersion of metal NPs. The shift of Pt and Pd binding energy reveals the presence of a chemical interaction between metal NPs and nitrogen defects, especially in the case of Pd. All the catalysts were characterized by electrochemical techniques, showing the general superiority of metal NPs loaded on doped MC, with respect to the same amount and type of metal deposited on undoped MC-2. In particular, Pt nanoparticles supported on N-doped supports showed high activities for the ORR in acidic solutions, with better performances than those of commercial Pt@vulcan (30 wt % Pt on Vulcan XC-72). Furthermore, Pt NPs loaded on mesoporous carbon seems to possess higher stability with respect to the standard Pt@vulcan. This was rationalized in term of a better confinement effect inside the mesoporous structure. In conclusion, the doped mesoporous carbon supports prepared in this work represent a viable tool for the preparation of new electrocatalysts characterized by good activities, a key factor in future fuel cell technology.

AUTHOR INFORMATION

Corresponding Author

*C. Durante. Tel.: +39 049 8275112. Fax: +39 049 8275829. E-mail: christian.durante@unipd.it.

Notes

The authors declare no competing financial interest.

ACKNOWLEDGMENTS

The research leading to these results has received funding from the University of Padova (PRAT CPDA139814/13) and the Fuel Cells and Hydrogen Joint Undertaking (FCH-JU) within the CathCat project under contract No. 303492. M.F. thanks Fondazione Cariparo for a Ph.D. fellowship.

REFERENCES

(1) Mayrhofer, K. J. J.; Arenz, M. Improvements to the Efficiency and Lifetime of Polymer Electrolyte Membrane Fuel Cells Can Be Realized by Finding More Active and Stable Electrocatalytic Cathode Materials. A Computational Search Has Found Two Such Alloys and Confirmed Their Enhanced Properties Experimentally. *Nat. Chem.* **2009**, *1*, 518−519.

(2) Jung, H. G.; Hassoun, J.; Park, J. B.; Sun, Y. K.; Scrosati, B. An Improved High-Performance Lithium-Air Battery. *Nat. Chem.* **2012**, *4*, 579−585.

(3) Liu, C. W.; Wei, Y. C.; Wang, K. W. Surface Condition Manipulation and Oxygen Reduction Enhancement of PtAu/C Catalysts Synergistically Modified by CeO_2 Addition and N_2 Treatment. *J. Phys. Chem. C* **2011**, *115*, 8702−8708.

(4) Favaro, M.; Perini, L.; Agnoli, S.; Durante, C.; Gennaro, A.; Granozzi, G. Palladium Nanoparticles Supported on Nitrogen-Doped HOPG: A Surface Science and Electrochemical Study. *Phys. Chem. Chem. Phys.* **2013**, *15*, 2923−2931.

(5) Perini, L.; Durante, C.; Favaro, M.; Agnoli, S.; Granozzi, G.; Gennaro, A. Electrocatalysis at Palladium Nanoparticles: Effect of The Support Nitrogen Doping on the Catalytic Activation of Carbon-Halogen Bond. *Appl. Catal., B* **2014**, *144*, 300−307.

(6) Leiva, E.; Iwasita, T.; Herrero, E.; Feliu, J. M. Effect of Adatoms in the Electrocatalysis of HCOOH Oxidation. A Theoretical Model. *Langmuir* **1997**, *13*, 6287−6293.

(7) Smith, S. P. E.; Abrunã, H. D. Structural Effects on the Oxidation of HCOOH by Bismuth Modified Pt(111) Electrodes with (110) Monatomic Steps. *J. Electroanal. Chem.* **1999**, *467*, 43−49.

(8) Wei, J.; Zhou, D.; Sun, Z.; Deng, Y.; Xia, Y.; Zhao, D. A Controllable Synthesis of Rich Nitrogen-Doped Ordered Mesoporous Carbon for CO_2 Capture and Supercapacitors. *Adv. Funct. Mater.* **2013**, *23*, 2322−2328.

(9) Alegre, C.; Gálvez, M. E.; Baquedano, E.; Moliner, R.; Pastor, E.; Lázaro, M. J. Oxygen-Functionalized Highly Mesoporous Carbon Xerogel based Catalysts for Direct Methanol Fuel Cell Anodes. *J. Phys. Chem. C* **2013**, *117*, 13045−13058.

(10) Lin, M. L.; Lo, M. Y.; Mou, C. Y. PtRu Nanoparticles Supported on Ozone-Treated Mesoporous Carbon Thin Film as Highly Active Anode Materials for Direct Methanol Fuel Cells. *J. Phys. Chem. C* **2009**, *113*, 16158−16168.

(11) Favaro, M.; Agnoli, S.; Ferrighi, L.; Colazzo, L.; Di Valentin, C.; Durante, C.; Sedona, F.; Sambi, M.; Gennaro, A.; Granozzi, G. Single and Multiple Doping in Graphene Quantum Dots: Unraveling the Origin of Selectivity in the Oxygen Reduction Reaction. *ACS Catal.* **2015**, *5*, 129−144.

(12) Zhang, J.; Kong, L. B.; Cai, J. J.; Luo, Y. C.; Kang, L. Nano-Composite of Polypyrrole/Modified Mesoporous Carbon for Electrochemical Capacitor Application. *Electrochim. Acta* **2010**, *55*, 8067−8073.

(13) Maldonado, S.; Stevenson, K. J. Influence of Nitrogen Doping on Oxygen Reduction Electrocatalysis at Carbon Nanofiber Electrodes. *J. Phys. Chem. B* **2005**, *109*, 4707−4716.

(14) Wu, J.; Yang, Z.; Li, V.; Sun, Q.; Jin, C.; Strasserd, P.; Yang, R. Phosphorus-Doped Porous Carbons as Efficient Electrocatalysts for Oxygen Reduction. *J. Mater. Chem. A* **2013**, *1*, 9889−9896.

(15) Qu, L.; Liu, Y.; Baek, J. B.; Dai, L. Nitrogen-Doped Graphene as Efficient Metal-Free Electrocatalyst for Oxygen Reduction in Fuel Cells. *ACS Nano* **2010**, *4*, 1321−1326.

(16) Liang, H. W.; Wei, W.; Wu, Z. S.; Feng, X.; Müllen, K. Communication Mesoporous Metal−Nitrogen-Doped Carbon Electrocatalysts for Highly Efficient Oxygen Reduction Reaction. *J. Am. Chem. Soc.* **2013**, *135*, 16002−16005.

(17) Sheng, Z. H.; Shao, L.; Chen, J. J.; Bao, W. J.; Wang, F. B.; Xia, X. H. Catalyst-Free Synthesis of Nitrogen-Doped Graphene via Thermal Annealing Graphite Oxide with Melamine and Its Excellent Electrocatalysis. *ACS Nano* **2011**, *5*, 4350−4358.

(18) Zhou, Y.; Pasquarelli, R.; Holme, T.; Berry, J.; Ginley, D.; O'Hayre, R. Improving PEM Fuel Cell Catalyst Activity and Durability Using Nitrogen-Doped Carbon Supports: Observations from Model Pt/HOPG Systems. *J. Mater. Chem.* **2009**, *19*, 7830−7838.

(19) Kumar, S. M. S.; Herrero, J. S.; Irusta, S.; Scott, K. The Effect of Pretreatment of Vulcan XC-72R Carbon on Morphology and Electrochemical Oxygen Reduction Kinetics of Supported Pd Nano-Particle in Acidic Electrolyte. *J. Electroanal. Chem.* **2010**, *647*, 211−221.

(20) Wei, D.; Liu, Y.; Wang, Y.; Zhang, H.; Huang, L.; Yu, G. Synthesis of N-Doped Graphene by Chemical Vapor Deposition and Its Electrical Properties. *Nano Lett.* **2009**, *9*, 1752−1758.

(21) Wang, T. S.; Ding, J. J.; Cheng, R.; Peng, H. B.; Lu, X.; Zhao, Y. T. Diamond-like Carbon Produced by Highly Charged Ions Impact on Highly Oriented Pyrolytic Graphite. *Nucl. Instrum. Methods Phys. Res., Sect. B* **2012**, *272*, 15−17.

(22) Barinov, A.; Malcioglu, O. B.; Fabris, S.; Sun, T.; Gregoratti, L.; Dalmiglio, M.; Kiskinova, M. Initial Stages of Oxidation on Graphitic Surfaces: Photoemission Study and Density Functional Theory Calculations. *J. Phys. Chem. C* **2009**, *113*, 9009−9013.

(23) Zhang, C.; Fu, L.; Liu, N.; Liu, M.; Wang, Y.; Liu, Z. Synthesis of Nitrogen-Doped Graphene Using Embedded Carbon and Nitrogen Sources. *Adv. Mater.* **2011**, *23*, 1020−1024.

(24) Usachov, D.; Vilkov, O.; Grüneis, A.; Haberer, D.; Fedorov, A.; Adamchuk, V. K.; Preobrajenski, A. B.; Dudin, P.; Barinov, A.; Oehzelt,

DOI: 10.1021/am506916y
ACS Appl. Mater. Interfaces 2015, 7, 1170−1179

M.; Laubschat, C.; Vyalikh, D. V. Nitrogen-Doped Graphene: Efficient Growth, Structure, and Electronic Properties. *Nano Lett.* **2011**, *11*, 5401−5407.
(25) Favaro, M.; Perini, L.; Agnoli, S.; Durante, C.; Granozzi, G.; Gennaro, A. Electrochemical Behavior of N and Ar Implanted Highly Oriented Pyrolytic Graphite Substrates and Activity Toward Oxygen Reduction Reaction. *Electrochim. Acta* **2013**, *88*, 477−487.
(26) Hellgren, N.; Guo, J.; Luo, Y.; Såthe, C.; Agui, A.; Kashtanov, S.; Nordgren, J.; Ågren, H.; Sundgren, J. E. Electronic Structure of Carbon Nitride Thin Films Studied by X-ray Spectroscopy Techniques. *Thin Solid Films* **2005**, *471*, 19−34.
(27) Pylypenko, S.; Queen, A.; Olson, T. S.; Dameron, A.; O-Neill, K.; Neyerlin, K. C.; Pivovar, B.; Dinh, H. N.; Ginley, D. S.; Gennet, T.; O-Hayre, R. Tuning Carbon-based Fuel Cell Catalyst Support Structures via Nitrogen Functionalization. I. Investigation of Structural and Compositional Modification of Highly Oriented Pyrolytic Graphite Model Catalyst Supports as a Function of Nitrogen Implantation Dose. *J. Phys. Chem. C* **2011**, *115*, 13667−13675.
(28) Dresselhaus, M. S.; Jorio, A.; Saito, R. Characterizing Graphene, Graphite, and Carbon Nanotubes by Raman Spectroscopy. *Annu. Rev. Condens. Matter Phys.* **2010**, *1*, 89−108.
(29) Zhao, Z.; Dai, Y.; Lin, J.; Wang, G. Highly-Ordered Mesoporous Carbon Nitride with Ultrahigh Surface Area and Pore Volume as a Superior Dehydrogenation Catalyst. *Chem. Mater.* **2014**, *26*, 3151−3161.
(30) Chen, Y.; Wang, J.; Liu, H.; Banis, M. N.; Li, R.; Sun, X.; Sham, T. K.; Ye, S.; Knights, S. Nitrogen Doping Effects on Carbon Nanotubes and the Origin of the Enhanced Electrocatalytic Activity of Supported Pt for Proton-Exchange Membrane Fuel Cells. *J. Phys. Chem. C* **2011**, *115*, 3769−3776.
(31) Jua, W.; Favaro, M.; Durante, C.; Perini, L.; Agnoli, S.; Schneider, O.; Stimming, U.; Granozzi, G. Pd Nanoparticles Deposited on Nitrogen-Doped HOPG: New Insights into the Pd-Catalyzed Oxygen Reduction Reaction. *Electrochim. Acta* **2014**, *141*, 89−101.
(32) Zhou, Y.; Holme, T.; Berry, J.; Ohno, T. R.; Ginley, D.; O'Hayre, R. Dopant-Induced Electronic Structure Modification of HOPG Surfaces: Implications for High Activity Fuel Cell Catalysts. *J. Phys. Chem. C* **2010**, *114*, 506−515.
(33) Zhou, Y.; Neyerlin, K.; Olson, T. S.; Pylypenko, S.; Bult, J.; Dinh, H. N.; Gennett, T.; Shao, Z.; O'Hayre, R. Enhancement of Pt and Pt-Alloy Fuel Cell Catalyst Activity and Durability via Nitrogen-Modified Carbon Supports. *Energy Environ. Sci.* **2010**, *3*, 1437−1446.
(34) Groves, M. N.; Chan, A. S. W.; Malardier-Jugroot, C.; Jugroot, M. Improving Platinum Catalyst Binding Energy to Graphene through Nitrogen Doping. *Chem. Phys. Lett.* **2009**, *481*, 214−219.
(35) Kim, N. D.; Kim, W.; Joo, J. B.; Oha, S.; Kim, P.; Kim, Y.; Yi, J. Electrochemical Capacitor Performance of N-Doped Mesoporous Carbons Prepared by Ammoxidation. *J. Power Sources* **2008**, *180*, 671−675.
(36) Hulicova, D.; Yamashita, J.; Soneda, Y.; Hatori, H.; Kodama, M. Supercapacitors Prepared from Melamine-based Carbon. *Chem. Mater.* **2005**, *17*, 1241−1247.
(37) Ania, C. O.; Khomenko, V.; Raymundo-Piñero, E.; Parra, J. B.; Béguin, F. The Large Electrochemical Capacitance of Microporous Doped Carbon Obtained by Using a Zeolite Template. *Adv. Funct. Mater.* **2007**, *17*, 1828−1828.
(38) Lota, G.; Lota, K.; Frackowiak, E. Nanotubes based Composites Rich in Nitrogen for Supercapacitor Application. *Electrochem. Commun.* **2007**, *9*, 1828−1823.
(39) Jia, N.; Wang, Z.; Yang, G.; Shen, H.; Zhu, L. Electrochemical Properties of Ordered Mesoporous Carbon and Its Electroanalytical Application for Selective Determination of Dopamine. *Electrochem. Commun.* **2007**, *9*, 233−238.
(40) Musameh, M.; Wang, J.; Merkoci, A.; Lin, Y. Low-Potential Stable NADH Detection at Carbon-Nanotube-Modified Glassy Carbon Electrodes. *Electrochem. Commun.* **2002**, *4*, 743−746.
(41) Ikeda, T.; Boero, M.; Huang, S. F.; Terakura, K.; Oshima, M.; Ozaki, J. Carbon Alloy Catalysts: Active Sites for Oxygen Reduction Reaction. *J. Phys. Chem. C* **2008**, *112*, 14706−14709.
(42) Wong, W. Y.; Daud, W. R. W.; Mohamad, A. B.; Kadhum, A. A. H.; Loh, K. S.; Majlan, E. H. Recent Progress in Nitrogen-Doped Carbon and Its Composites as Electrocatalysts For Fuel Cell Applications. *Int. J. Hydrogen Energy* **2013**, *38*, 9370−9386.
(43) Wang, D. W.; Su, D. Heterogeneous Nanocarbon Materials for Oxygen Reduction Reaction. *Energy Environ. Sci.* **2014**, *7*, 576−591.
(44) Yang, Z.; Nie, H.; Chen, X.; Chen, X.; Huang, S. Recent Progress in Doped Carbon Nanomaterials as Effective Cathode Catalysts for Fuel Cell Oxygen Reduction Reaction. *J. Power Sources* **2013**, *236*, 238−249.
(45) Lai, L.; Potts, J. R.; Zhan, D.; Wang, L.; Poh, C. K.; Tang, C.; Gong, H.; Shen, Z.; Lin, J.; Ruoff, R. S. Exploration of the Active Center Structure of Nitrogen-Doped Graphene-based Catalysts for Oxygen Reduction Reaction. *Energy Environ. Sci.* **2012**, *5*, 7936−7942.
(46) Xing, T.; Zheng, Y.; Li, L. H.; Cowie, B. C. C.; Gunzelmann, D.; Qiao, S. Z.; Huang, S.; Chen, Y. Observation of Active Sites for Oxygen Reduction Reaction on Nitrogen-Doped Multilayer Graphene. *ACS Nano* **2014**, *8*, 6856−6862.
(47) Gottesfeld, S.; Raistrick, I. D.; Srinivasan, S. Oxygen Reduction Kinetics on a Platinum RDE Coated with a Recast Nafion Film. *J. Electrochem. Soc.* **1987**, *134*, 1455−1462.
(48) Song, C.; Zhang, J. In *PEM Fuel Cell Electrocatalyst and Catalyst Layers Fundamentals and Applications*; Zhang, J., Ed.; Springer-Verlag, London, 2008.
(49) Schmidt, J.; Gasteiger, H. A.; Stab, G. D.; Urban, P. M.; KoIb, D. M.; Behm, R. J. Characterization of High-Surface-Area Electrocatalysts Using a Rotating Disk Electrode Configuration. *J. Electrochem. Soc.* **1998**, *145*, 2354−2358.
(50) Pozio, A.; De Francesco, M.; Cemmi, A.; Cardellini, F.; Giorgi, L. Comparison of High Surface Pt/C Catalysts by Cyclic Voltammetry. *J. Power Sources* **2002**, *105*, 13−19.
(51) Zecevic, S. K.; Wainright, J. S.; Litt, M. H.; Gojkovic, S. L.; Savinell, R. F. Kinetics of O_2 Reduction on a Pt Electrode Covered with a Thin Film of Solid Polymer Electrolyte. *J. Electrochem. Soc.* **1997**, *144*, 2973−2982.
(52) Ferreira, P. J.; la O', G. J.; Shao-Horn, Y.; Morgan, D.; Makharia, R.; Kocha, S.; Gasteiger, H. A. Instability of Pt/C Electrocatalysts in Proton Exchange Membrane Fuel Cells. *J. Electrochem. Soc.* **2005**, *152*, A2256−A2271.

DOI: 10.1021/am506916y
ACS Appl. Mater. Interfaces 2015, 7, 1170−1179